Acta Geotechnica (2024) 19:4503–4518
https://doi.org/10.1007/s11440-023-02169-9

RESEARCH PAPER

Effect of particle shape on cyclic liquefaction resistance of granular materials

Sounik K. Banerjee[1] · Ming Yang[2] · Mahdi Taiebat[1]

Received: 28 August 2023 / Accepted: 16 November 2023 / Published online: 7 January 2024

Abstract
This study adopts three-dimensional discrete element method to examine how particle shape affects the cyclic liquefaction resistance of granular materials. A family of superquadric particles is employed to model different particle shapes by varying two shape parameters: aspect ratio (AR) and blockiness (B). Five smooth and convex particle shapes are considered in this study, with AR ranging from 0.5 to 1.5, and B varying from 2 to 8. These particles are used to create isotropically compressed samples at an initial confinement of 100 kPa and two relative densities (D_r) of 20% and 50%, resulting in ten samples. These samples are then subjected to constant-volume cyclic simple shearing with various levels of cyclic stress ratios until initial liquefaction occurs in 41 simulations. The results of these simulations reveal that at $D_r = 20\%$, the spherical particles exhibit the highest liquefaction resistance compared to the non-spherical particles. However, this trend is reversed for the samples with $D_r = 50\%$. By employing the overall regularity (OR) as a synthetic descriptor of particle shape, it is observed that liquefaction strength generally increases with higher OR at $D_r = 20\%$, while it demonstrates an approximately decreasing trend at $D_r = 50\%$. Furthermore, the initial coordination number and two critical state parameters based on the void ratio and the coordination number at the pre-shearing state of the samples, demonstrate a strong correlation with the cyclic liquefaction resistance within the ranges of particle shape and D_r considered in this study.

Keywords Cyclic liquefaction · Discrete element method · Granular material · Particle shape · State parameter

1 Introduction

Cyclic liquefaction of cohesionless soils can lead to a considerable accumulation of shear strains and, therefore deformations, posing risks to the supported infrastructure. Many factors, including soil type, consolidation state, and drainage condition, can influence soil cyclic behavior and accelerate or slow down the process of approaching liquefaction [e.g., 12, 48, 13, 23, 49, 54]. Understanding the impact of these factors is valuable for assessing and potentially enhancing the effectiveness of current constitutive models when simulating the cyclic liquefaction of granular materials [e.g., 38, 59, 15, 51, 32]. Soil type encompasses particle or granular-level characteristics such as particle mineralogy, particle size distribution (PSD), and particle shape. An ideal investigation of the effect of these factors on the cyclic liquefaction resistance of granular materials would require the isolation of their impact—something that is very challenging, if at all possible, in the laboratory testing of soils. In particular, a systematic investigation of the particle shape effects on the cyclic liquefaction requires consideration of the particle shape characteristics in different samples while adequately excluding the influence of other factors such as particle mineralogy and PSD. As a result, the experimental studies assessing only the particle shape effects on sand liquefaction are very limited.

Vaid et al. [48] conducted multiple constant-volume cyclic simple shear tests on rounded Ottawa sand and an angular Tailings sand with similar PSD, to assess their liquefaction resistance. The results revealed that the

✉ Mahdi Taiebat
mtaiebat@civil.ubc.ca

1 Department of Civil Engineering, University of British Columbia, Vancouver, BC, Canada

2 Department of Civil and Environmental Engineering, Northwestern University, Evanston, IL, USA

angular sand exhibits significantly higher liquefaction resistance than the rounded one for samples consolidated at a low confining pressure of 200 kPa and with relative densities above 40%. At higher confining pressure, the liquefaction resistance of angular sand was higher or smaller than the rounded one, depending on the relative density. Hubler et al. [22] investigated the cyclic liquefaction resistance of rounded Pea Gravel and angular crushed limestone using constant-volume cyclic simple shear tests. They observed that under cyclic stress ratio (CSR) less than 0.10, increasing particle angularity enhanced liquefaction resistance; this enhancement was not clear for the tests under higher levels of CSR. Wei et al. [52] examined the liquefaction resistance of clean sands with the same particle size distribution but different particle shapes and found that cyclic resistance decreases with increasing the overall regularity of particles for the samples at the same void ratio. Rui et al. [44] compared the liquefaction resistance of calcareous sand, quartz sand, and steel balls through undrained triaxial tests at a high relative density of 70%. Their study demonstrated that samples composed of non-spherical particles accumulate excess pore pressure at a slower rate and require more cycles to liquefy than samples of spherical particles.

The aforementioned laboratory experimental studies provide a fundamental understanding of the impact of particle shape on cyclic liquefaction resistance. However, there are inconsistencies in the findings, which could be attributed to variations in soil types, test protocols, adopted liquefaction criteria, and, notably, the challenge of isolating the effect of particle shape from other important factors like surface roughness and particle size distribution, which are expected to influence the results significantly. To address these concerns, the utilization of idealized particles can be advantageous. While laboratory experiments can be conducted using particles with similar shapes, an alternative approach is the discrete element method (DEM), which is a valuable numerical method for investigating the sole effect of particle shape on the cyclic liquefaction resistance of granular materials. DEM also enables the extraction and analysis of particle-level information and insights, which reinforces the observations derived from the macroscopic response.

In the particle dynamics DEM, there are generally two approaches to consider the effect of particle shape. The first approach involves incorporating a rolling resistance model [e.g., 2, 53] into spherical particles. This allows for accounting for the additional resistance due to particle shape without explicitly simulating the particle morphology. An alternative approach is to use non-spherical particles, which approximate the particle shape geometry to some extent. For a comprehensive overview of modeling methodologies for non-spherical particles in DEM, one can refer to [18]. Some examples of explicitly modeling particle shape include superquadrics [55], polyhedrons [21], agglomerates [19], nonuniform rational B-Splines based particles [31], clumping of multiple spheres [29], and particle shape mapping via level-set imaging [27].

The effect of particle shape on the mechanical response of granular materials under monotonic shearing has been widely explored. For instance, previous studies have shown that critical state friction angle increases with an increase in the rolling friction coefficient of spherical particles [17] and particle elongation [4], or a decrease in the aspect ratio [56] and sphericity [37]. For the critical state line in the space of void ratio and mean effective stress, Nguyen et al. [37] reported similar locations for spheres and ellipsoids but higher locations for clusters. Jerves et al. [25] conducted a comprehensive investigation using LS-DEM to analyze the dependence of critical state parameters on sphericity, roundness, and regularity. The DEM studies related to particle shape and cyclic liquefaction are rather limited, including those on clumped circular elements [3], clumped spheres [29, 35], and imaging Hostun sand via LS-DEM [26]. None of these studies have specifically explored the effect of particle shape on the cyclic liquefaction resistance of granular materials.

To start addressing this research gap, the current study aims to investigate the effect of particle shape on cyclic liquefaction resistance using simple superquadrics. The superquadric particles are controlled by two shape descriptors, namely blockiness and aspect ratio. Isotropically consolidated samples composed of particles with distinct shapes are prepared at similar relative densities. These samples then undergo constant-volume cyclic simple shearing until initial liquefaction, enabling the determination of the cyclic liquefaction resistance. It is important to note that the cyclic simple shearing performed on isotropically compressed samples in this study simulates the cyclic torsional hollow-cylinder shear tests typically conducted in laboratory testing of soils on similarly prepared samples. The simplification of dealing with isotropically compressed samples reduces the complexity associated with the inherent anisotropy that would otherwise be present. Furthermore, micromechanical descriptors quantifying the inherent fabric prior to cyclic shearing are calculated and correlated with the liquefaction resistance. This approach aims to reveal universal relationships that hold irrespective of the particle shape and relative density.

2 DEM setup

An open-source DEM code for simulation of particle dynamics LIGGGHTS [28] is used in this paper. Superquadric particles are adopted to construct the granular assembly [39]. These particles interact with each other based on a soft-particle law, allowing for slight overlap at the contact point. The contact law between particles consists of a Hertzian normal model and a history-dependent tangential model with a Coulomb cut-off; details of the contact models can be found in [39]. These contact models involve parameters including the particle Young's modulus (E), Poisson's ratio (ν), coefficient of restitution (ϵ), and coefficient of tangential friction (μ). It should be noted that due to explicit consideration of particle shape, no rolling resistance model is considered in this study.

2.1 Description of particle shape

This study selects superquadrics over other options, such as polyhedrons and level-set imaging of real particle shapes, because of their simplicity and computational efficiency. Based on the continuous functional representation of superquadrics [8]:

$$F(x,y,z) \equiv \left(\left|\frac{x}{a}\right|^{n_2}+\left|\frac{y}{b}\right|^{n_2}\right)^{\frac{n_1}{n_2}}+\left|\frac{z}{c}\right|^{n_1}-1=0, \quad (1)$$

by setting $n_1 = n_2 = 2$, one can end up with the general functional form of a triaxial ellipsoid, defined only parameters a, b, and c, as illustrated in Fig. 1a. In this study, a and b are set equal, and the ratio between c and a (or b) is referred to as the aspect ratio (AR). The AR can vary between 0 and ∞, and increasing AR indicates an increase in particle elongation. The parameters n_1 and n_2 control the curvature of a superquadric particle. Here n_1 is set equal to n_2 for simplicity, also denoted as B, representing "blockiness" (B). This study only considers particles with B larger than 2, and increasing B makes the particle more cuboid-like. Figure 1b presents the geometry variations of superquadric particles by varying AR and B. The five particles in the shaded area represent the ones considered in this study.

Figure 2 depicts variations of two general shape descriptors, including roundness (R) and sphericity (S) for the two groups of superquadric particles considered in this study, namely varying AR by fixing $B = 2$ and varying B by fixing AR $= 1$. Here particle roundness is determined as the ratio of the average radius of curvature of the corners to the radius of curvature of the maximum inscribed sphere [50], and sphericity is determined as the radius ratio of the maximum inscribed and minimum circumscribed spheres. More details on determining these shape descriptors for superquadric particles can be found in [6]. Figure 2a indicates non-monotonous variations of R and S with increasing AR from 0.5 to 1.5, while Fig. 2b suggests that R and S increase with increasing B from 2. By examining the variation magnitudes of R and S with increasing AR or B, one can notice that R demonstrates higher sensitivity to the changes in B, whereas varying AR induces higher changes in S. Loosely speaking, AR is more related to S, and B is more related to R in a relative sense.

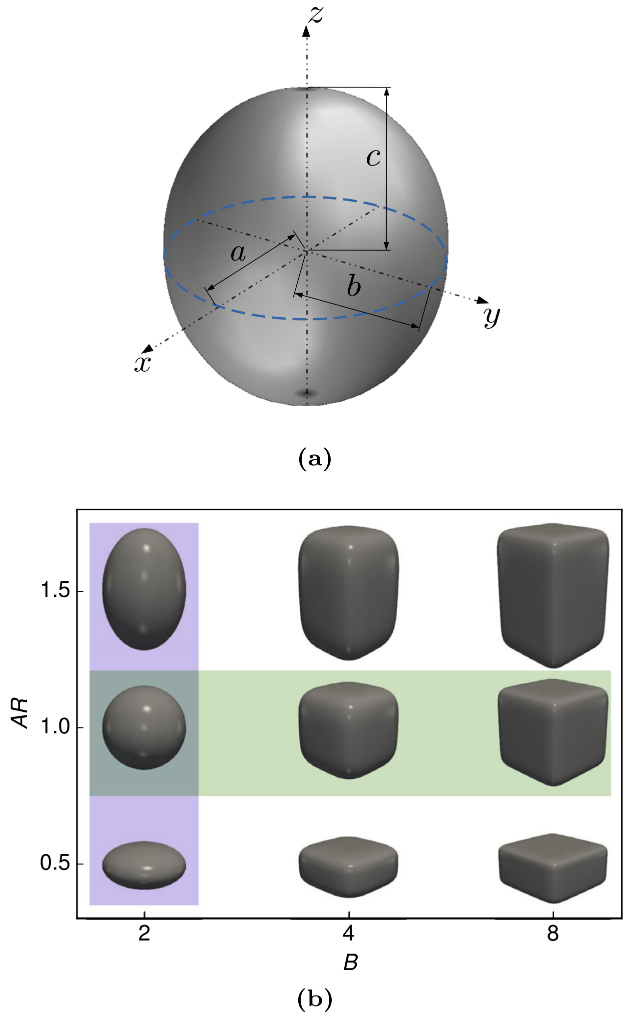

Fig. 1 **a** An ellipsoid generated from a superquadric particle by setting $n_1 = n_2 = 2$ with semi-axes a, b, and c; **b** shape variations of superquadric particles by changing aspect ratio (AR) and blockiness (B). Particles in shaded areas are the ones considered in this study

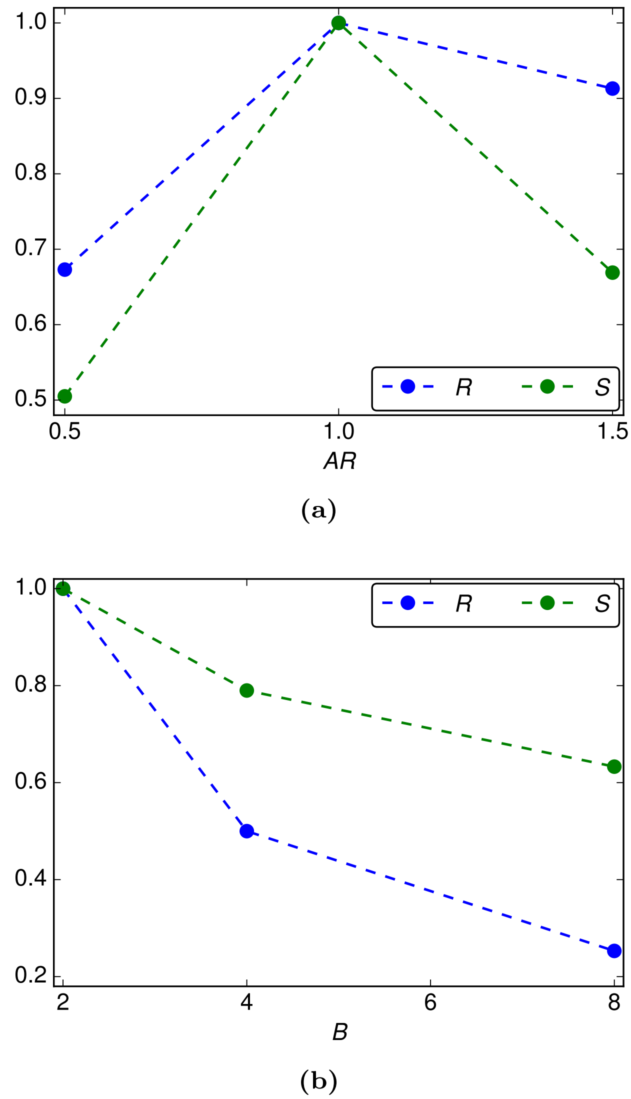

Fig. 2 Variations of roundness (R) and sphericity (S) for superquadric particles considered in this study and with varying **a** AR at $B = 2$ and **b** B at AR $= 1$

2.2 Sample preparation

DEM samples consisting of distinct superquadric particles are constructed following the same sample preparation protocol. The particle size distribution (PSD) exhibits a linear relation when plotted as the cumulative particle volume fraction against a logarithmic scale for particle size ($= 2a$). The PSD is characterized by a median particle size of 5 mm and the coefficient of uniformity of 2. Ten distinct classes of particles are constructed to approximate the continuous PSD. Each class comprises particles of the same size, and its number of particles is determined by the class volume and the particle size. One can refer to [36, 45] for the details of generating particles approximating a specified PSD. The study constructs isotropically consolidated DEM samples using the granular assembly consisting of 12, 400 particles. The DEM simulation parameters are given in Table 1.

To achieve isotropic compression of the particle assembly and reach a target mean stress p_0, a large cubic simulation box is created in LIGGGHTS. The box consists of rigid walls at the top and bottom sides, while the four lateral sides employ periodic boundaries, forming a bi-periodic cell. To prevent segregation during compression and subsequent shearing, gravity is disabled during both sample preparation and cyclic shearing stages. The particles are randomly inserted into the bi-periodic cell, ensuring there is no overlap between them due to the sufficiently large dimensions of the cell. Once the insertion process is complete, a servo-control algorithm [e.g., 47] is employed to isotropically compress the sample to 10% of the target value p_0. During this initial compression stage, the tangential friction coefficient μ_{prep} is set to different values from the $\mu = 0.5$ listed in Table 1. Subsequently, μ is set to 0.5, as specified in Table 1, and the sample is further isotropically compressed to reach the target value of p_0 (set at 100 kPa for this study) using servo-control. The value of μ is retained as 0.5 during the subsequent cyclic shearing stage. This two-step isotropic compression procedure, adapted from [47], is a numerical technique employed to obtain samples with different densities, and has also been utilized in other recent studies [7, 60–63]. By setting μ_{prep} to 0 and 0.5 in the first step of isotropic compression, samples with extreme void ratios are obtained, typically representing the loosest and densest achievable states, respectively. These extreme void ratios are regarded as the minimum void ratio $e_{\min}$ and maximum void ratio $e_{\max}$ for the sole purpose of calculating the relative densities of the samples.

Figure 3 presents the simulated values of $e_{\max}$ and $e_{\min}$ obtained in this study. No comparison is made here since the authors are not aware of other relevant studies reporting these extreme void ratios under similar settings. One can see how the extreme void ratios change as AR or B varies, demonstrating the importance of considering relative density D_{r} rather than void ratio e when analyzing the effect of

Table 1 DEM parameters

Description	Value
Particle density, ρ	2500 kg/m^3
Particle Young's modulus, E	70 GPa
Particle Poisson's ratio, v	0.25
Tangential friction coefficient, μ	0.5
Restitution coefficient, ϵ	0.2

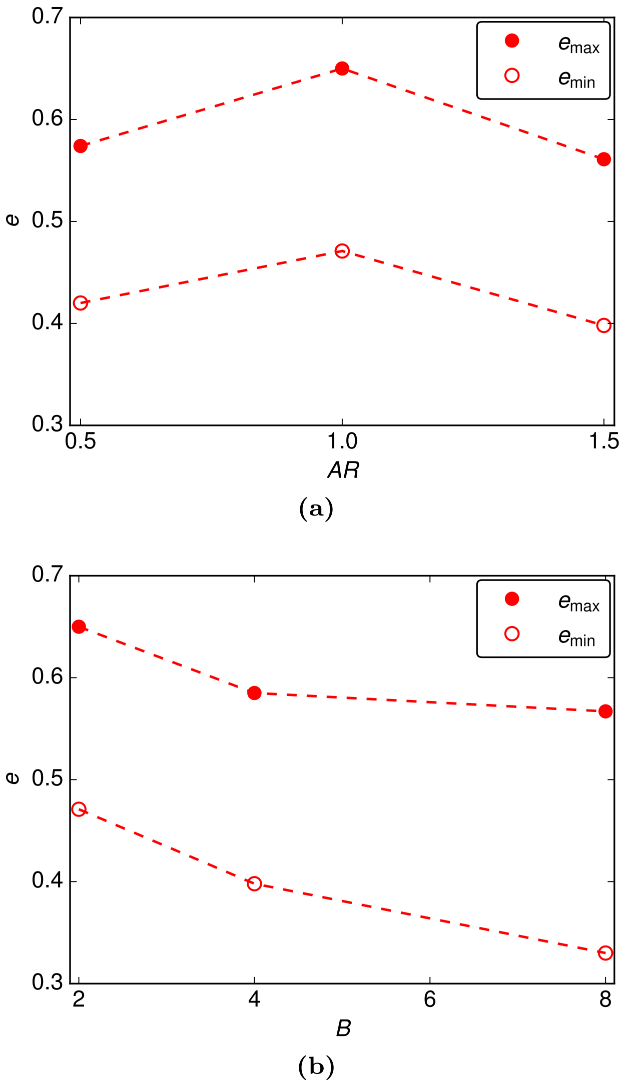

Fig. 3 Calculated maximum and minimum void ratios of the samples with different values of **a** AR at B =2, and **b** B at AR =1

particle shape. On that basis, for each type of superquadric particle, samples with two target relative densities of D_r = 20% and 50% are constructed to high accuracy by exploiting the value of μ_{prep} iteratively in the range of 0 and 0.5. Therefore, in total, ten samples are prepared covering five distinct particle shapes and two levels of D_r, all isotropically compressed to $p_0 = 100$ kPa. It must be noted that using these reduced friction coefficients tends to construct DEM samples with relatively high contact density, compared with samples prepared at similar D_r using typical laboratory sample preparation techniques [1]. This effect becomes more pronounced with increasing the sample density. Thus the dense DEM samples following the current sample preparation protocol will manifest considerably higher liquefaction resistance than one would expect from physical tests in the laboratory. Therefore, in this study, DEM samples with D_r larger than 50% are not considered. As such, the DEM samples with $D_r = 50\%$ in this study are not comparable to the laboratory ones at the same relative density, given the difference in sample preparation methods; rather, they may be compared with very dense samples prepared in the laboratory. The DEM samples with $D_r = 20\%$ correspond to medium-dense samples prepared in the laboratory. To reduce the high contact density in the dense DEM samples, one can refer to [58] for alternative numerical schemes. Table 2 provides the constructed sample properties, including the tangential friction coefficient μ_{prep} for preparing the sample, the void ratio at the end of isotropic compression, and some other descriptors to be explained later in the paper. Figure 4 shows snapshots of the samples with different superquadric particles and $D_r = 50\%$. Figure 5a displays a sample with spheres isotropically compressed to $D_r = 50\%$ and $p_0 = 100$ kPa.

2.3 Shearing process

In the cyclic shearing stage, the sample volume is kept constant by fixing the four lateral periodic boundaries and the bottom wall, and keeping the sample height h constant. Cyclic simple shearing is imposed by moving the top wall horizontally along the x axis at a constant velocity denoted as v_x in forward and backward directions, as shown in Fig. 5b. To eliminate slippage between the walls and the sample, a layer of particles is glued to the top and bottom walls, as shown in this figure. The resulting imposed shear strain $\gamma = \gamma_{xz}$ has a sawtooth pattern with the direction of shearing reversed each time the shear stress $\tau = \tau_{xz}$ reaches the target amplitude τ^{amp} as shown in Fig. 5c. The cyclic

Table 2 Properties of samples isotropically compressed at $p_0 = 100$ kPa

AR	B	μ_{prep}	e_0	D_r(%)	z_0	e_{cs}	z_{cs}
0.5	2	0.275	0.450	20	4.66	0.669	4.48
0.5	2	0.178	0.498	50	6.45	0.668	4.42
1.0	2	0.281	0.513	20	4.73	0.623	4.52
1.0	2	0.181	0.563	50	5.23	0.622	4.52
1.5	2	0.268	0.433	20	4.38	0.614	4.59
1.5	2	0.162	0.483	50	6.74	0.613	4.61
1.0	4	0.264	0.439	20	4.67	0.581	4.68
1.0	4	0.143	0.495	50	5.97	0.580	4.69
1.0	8	0.261	0.383	20	4.64	0.468	4.78
1.0	8	0.134	0.454	50	6.01	0.469	4.76

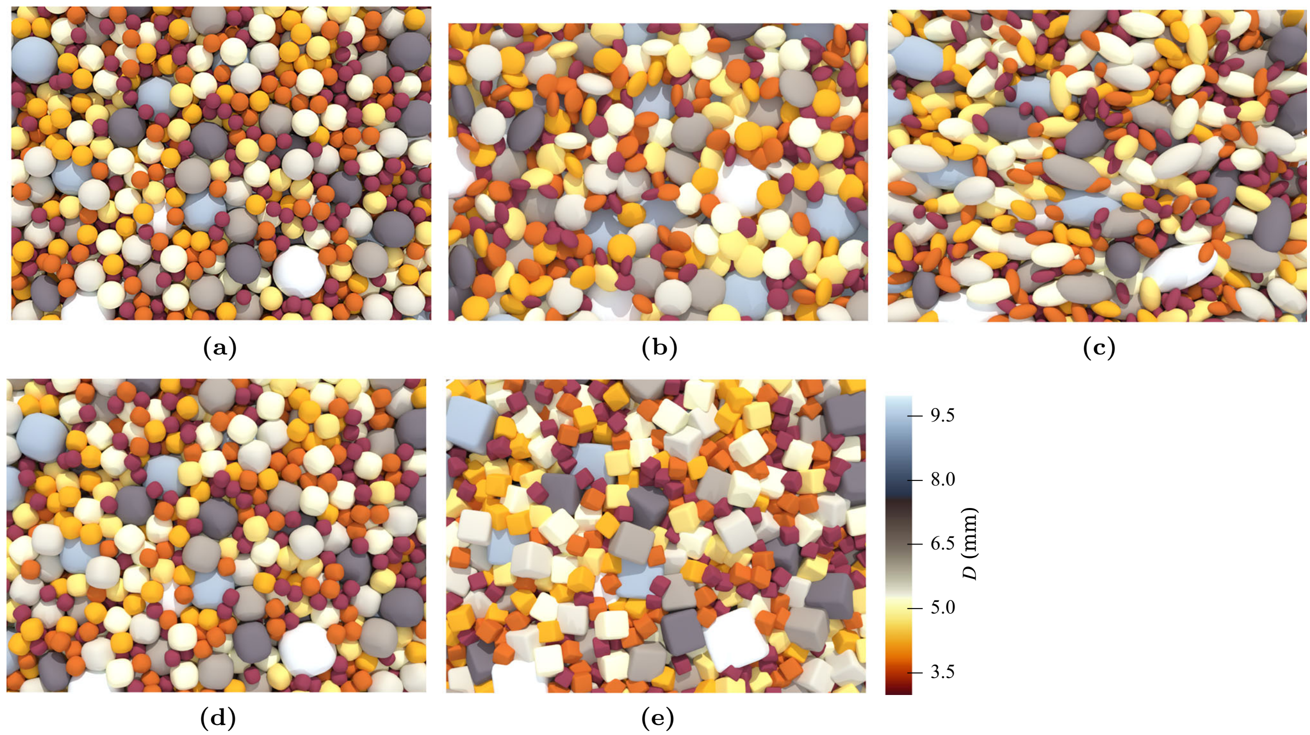

Fig. 4 Snapshots of samples with different superquadric particles corresponding to **a** AR = 1, $B = 2$, **b** AR = 0.5, $B = 2$, **c** AR = 1.5, $B = 2$, **d** AR = 1, $B = 4$, and **e** AR = 1, $B = 8$, isotropically compressed to p_0 = 100 kPa and D_r = 50%

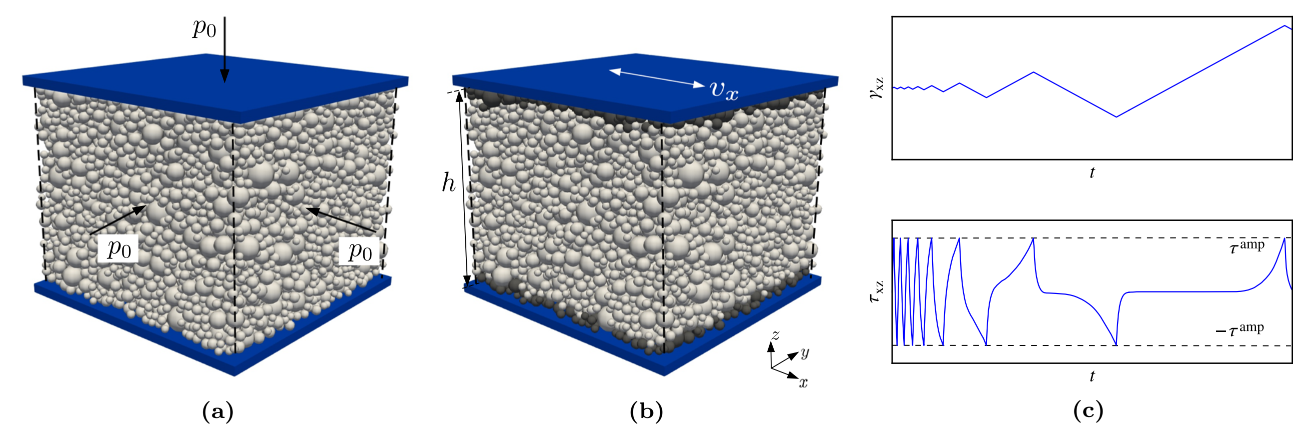

Fig. 5 Schematic representation of particle arrangements and boundary condition for one of the tests: **a** at the end of sample preparation under isotropic compression, and **b** during the constant volume cyclic shearing, with the gray particles glued to the top and bottom walls of the simulation box; **c** loading protocol for the cyclic simple shear with uniform CSR

shearing intensity is quantified by the dimensionless quantity cyclic stress ratio (CSR), defined as

$$\mathrm{CSR} = \frac{\tau^{\mathrm{amp}}}{p_0}. \tag{2}$$

The rate of shearing is chosen with special attention to the inertial number $I = \dot{\gamma} d\sqrt{\rho/p}$, where $\dot{\gamma} = |v_x|/h$ represents the shear strain rate, ρ is the particle density, d is the mean particle size, and v_x denotes the shear velocity. The shearing is regarded as nearly quasistatic if $I \ll 1$, and the threshold is typically chosen as 10^{-3} [34]. This study does not maintain a constant I throughout the shearing process; instead, shearing is induced by moving the top wall at a constant velocity of 0.01 m/s. This approach ensures that I consistently remains below 10^{-3} prior to the occurrence of sample liquefaction. It is, however, important to note that I may exceed this threshold during the sample liquefaction due to unstable deformation and a significant decrease in p, as observed in previous DEM studies [33, 62, 63]. Such behavior is an intrinsic feature of cyclic liquefaction only and is not influenced by variations in the shear rate. It must be noted that in these studies, p never reaches zero, and in turn, I remains less than 0.1 even within the liquefaction regime.

The momentum transmission from the top wall particles to the mobile particles of the sheared sample was visualized by dividing the sample into ten layers along the z direction. As demonstrated in [7], the average shear velocity $\langle v_x \rangle$ of particles in each layer was observed to follow a nearly linear distribution along the z axis before soil liquefaction occurred. However, this linear relation might deteriorate after soil liquefaction, as the collapse of the well-connected contact network leads to certain non-homogeneities. An alternative shearing protocol, not explored in the present study, would involve employing Lees-Edwards boundary conditions [10, 30] to enforce a desired linear relation between $\langle v_x \rangle$ and z.

The simulated constant-volume cyclic simple shear tests are summarized in Table 3. For each sample, at least four CSR values are considered, each leading to a cyclic simple shear simulation. These CSR values are carefully selected to induce initial liquefaction within approximately 100 loading cycles. These numerical experiments enable a systematic analysis of the influence of particle shape on the cyclic liquefaction resistance of granular materials. The simulations were performed using the DesignSafe cyber-infrastructure [43], a web-based research and computation platform for the natural hazard engineering community.

3 Macroscopic response

The homogenized stress tensor at the sample scale is used to characterize the overall mechanical response of a particle assembly under constant volume cyclic shearing. Over a given volume V, the stress tensor $\boldsymbol{\sigma}$ is calculated as a function of the micro-scale interactions between particles as:

Table 3 Simulated constant volume cyclic simple shear tests on samples with different AR, B, D_r, and CSR

AR	B	D_r (%)	CSR
0.5	2	20	0.10, 0.15, 0.20, 0.25
		50	0.25, 0.35, 0.45, 0.55
1.0	2	20	0.10, 0.15, 0.20, 0.25
		50	0.25, 0.35, 0.45, 0.55
1.5	2	20	0.10, 0.15, 0.20, 0.25
		50	0.25, 0.35, 0.45, 0.55
1.0	4	20	0.10, 0.15, 0.20, 0.25
		50	0.25, 0.35, 0.45, 0.55
1.0	8	20	0.05, 0.10, 0.15, 0.20, 0.25
		50	0.25, 0.35, 0.45, 0.55

$$\boldsymbol{\sigma} = \frac{1}{V}\sum_{i \in N_c} \boldsymbol{l}^i \otimes \boldsymbol{f}^i, \tag{3}$$

where the branch vector $\boldsymbol{l}^i$ connects the centers of two particles, $\boldsymbol{f}^i$ is the contact force, $\otimes$ refers to the tensor dyadic product, and the summation includes all the contacts N_c in the selected volume V. In the simple shear test, the shear stress τ and the mean effective stress p are given by $\tau = \sigma_{xz}$ and $p = (\sigma_{xx} + \sigma_{yy} + \sigma_{zz})/3$, respectively.

Pore water is not explicitly simulated in this study because previous laboratory experiments [16] and numerical simulations [11, 64, 65] have consistently shown the equivalence between the “truly undrained test” (a liquid-saturated sample subjected to constant total stress conditions) and the “constant-volume test“ (a dry sample under constant volume condition). This study adopts the constant-volume approach due to its simplicity and low computational cost. In the constant-volume approach, the homogenized stress via Eq. (3) corresponds to the effective stress in the truly undrained test. The initial confinement p_0 is the unchanged total mean stress in the truly undrained test. Thus, the deduced excess pore pressure in the equivalent truly undrained system with an incompressible pore fluid can be computed as the variation of the simulated reduction in mean effective stress:

$$\Delta u = p_0 - p, \tag{4}$$

and subsequently, the dimensionless excess pore pressure ratio would be:

$$r_u = \frac{\Delta u}{p_0} = 1 - \frac{p}{p_0}. \tag{5}$$

It is worth noting that the equivalence between the truly undrained and constant volume tests may require reevaluation when the sample undergoes liquefaction. In such instances, the hydrodynamic forces arising from solid–fluid interactions might become more pronounced compared to the low-contact forces, potentially impacting the motion of particles. This influence could extend to the point where the sample exits the liquefaction regime. Addressing this concern goes beyond the scope of the current study and will be explored in future research.

The shear strain γ is measured as:

$$\gamma = \frac{x_\mathrm{W}}{h}, \tag{6}$$

where x_W refers to the cumulative horizontal displacement of the top wall along x direction.

For the adopted loading protocol with constant $\dot{\gamma}$ between the shear reversals at $\pm\tau^{\mathrm{amp}}$, the time interval $T/2$ between two successive shear reversals varies in different shearing cycles, as shown in Fig. 5c. Considering $T(N)$ as the duration of cycle N and t_N its initial time, to present the evolution of a quantity such as r_u, a "fractional cycle number" N' is used to replace the current running time t by interpolation between two successive cycles:

$$N' = N + \frac{t - t_N}{T(N)} \tag{7}$$

where N is the cycle number, t_N is the starting time for the Nth cycle, and $T(N)$ is the duration of cycle N. The value of N' coincides with N at $t = t_N$, and increases by one unit at $t = t_N + T$. To avoid confusion, hereafter, the symbol N is used to represent fractional cycle number as defined by N'.

3.1 Stress and strain response

Figure 6 illustrates the typical macroscopic behavior of a constant-volume cyclic simple shear test conducted on a sample composed of ellipsoidal particles with $\mathrm{AR} = 1.5$ and $B = 2$ at $D_\mathrm{r} = 20\%$ and under $\mathrm{CSR} = 0.20$. This figure showcases the stress path, stress–strain curve, and the evolutions of excess pore pressure ratio and shear strain with the number of loading cycles. The stress path begins at $p = 100$ kPa and $\tau = 0$ kPa, while the stress–strain curves start from the origin. The stress path moves up and down periodically around $\tau = 0$ and between $\pm\tau^{\mathrm{amp}}$, and exhibits a general decreasing trend of p (or increasing of r_u), as shown in Fig. 6a, c, indicating an overall contraction tendency of the granular system. As the loading cycles progress, one can also one can observe local fluctuations of p at each loading cycle, where increasing corresponds to dilation tendency and decreasing corresponds to contraction tendency. Shear strain γ oscillates around $\gamma = 0$, with increasing cyclic amplitude as the shearing progresses, as shown in Fig. 6b, d. Eventually, in the ninth loading cycle, p momentarily drops to very small values close to 0, or r_u gets close to 1.0, i.e., the sample liquefies, and cyclic shear strains accumulate. This is the semifliuidized state described by [9]. While some of the DEM simulations may not reach r_u of 1.0, at $r_u \geq 0.95$, all simulations exhibit fluid-

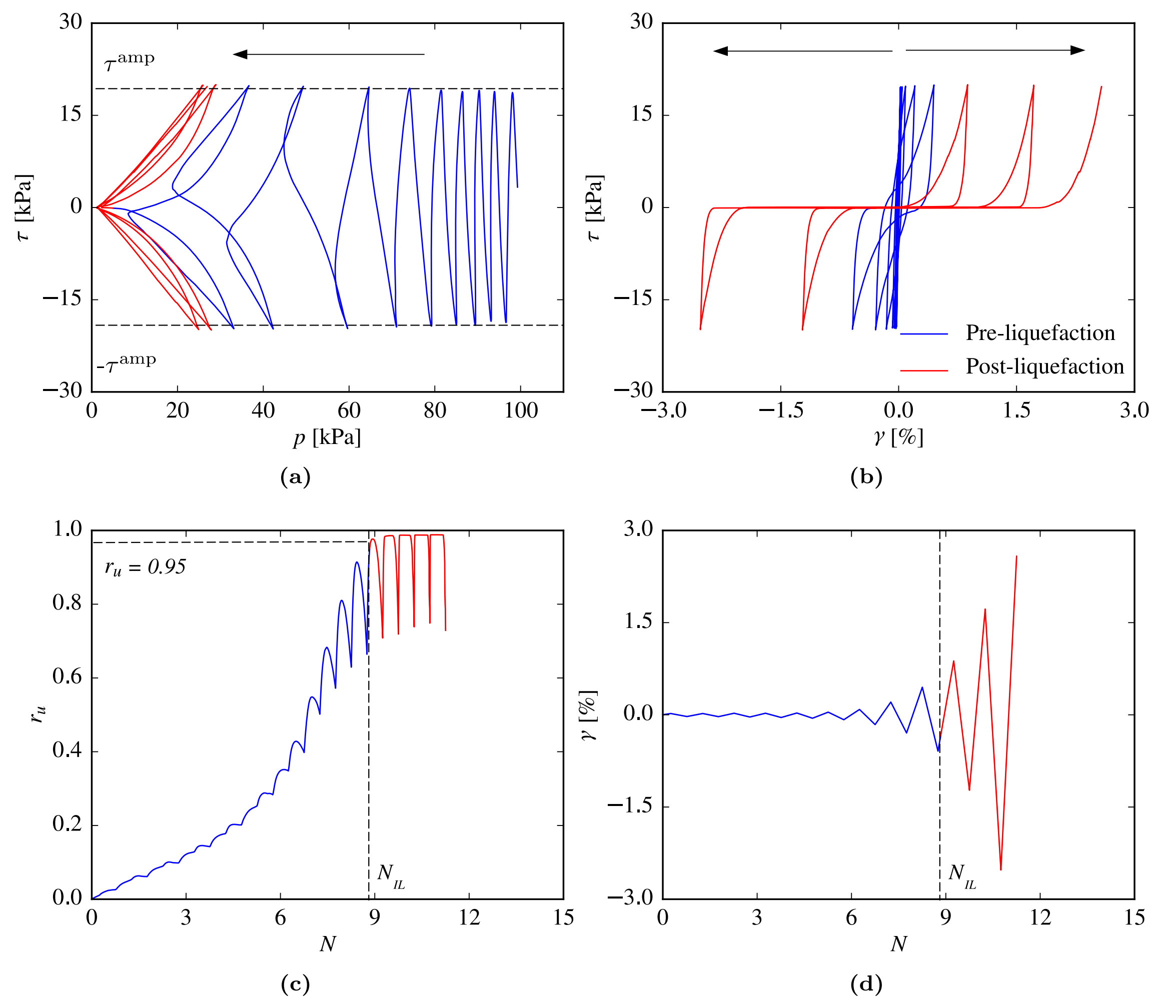

Fig. 6 Macroscopic response of constant volume cyclic simple shear test on a sample with AR = 1.5 and $B = 2$ and at D_r = 30%, subjected to CSR = 0.20: **a** stress path, **b** stress–strain curve, **c** derived excess pore pressure evolution, and **d** shear strain development. N_{IL} is the number of cycles to reach initial liquefaction at $r_u \geq 0.95$, dividing the response into pre- and post-liquefaction

like behavior characterized by substantial shear strain development. Consequently, the first occurrence of r_u exceeding 0.95 is denoted as initial liquefaction (IL) in this study, and the corresponding number of cycles to reach this state is denoted as N_{IL}, as shown in Fig. 6c. Shearing periods before and after initial liquefaction are commonly referred to as pre- and post-liquefaction, respectively. The liquefaction or semifluidized state is characterized by a loss of stability or load-bearing capacity, leading to significant shear strain accumulation near $\tau \simeq 0$, as depicted in Fig. 6b. During this stage, the granular system undergoes substantial shear strains while gradually rebuilding the contact network, as described by [63]. Eventually, the contact network becomes strong enough to shift the stress path away from the liquefied state. The stress path then evolves along the failure envelope, exhibiting noticeable dilation before τ reaches the prescribed amplitude. The subsequent stress path due to reverse loading contributes to the formation of the typical butterfly shape. In contrast to the increasing magnitude of shear strain observed in the semifluidized state in subsequent loading cycles, the shear strain developed during the dilation periods does not exhibit significant changes in different post-liquefaction cycles. These observations are consistent with other laboratory experiments and DEM studies.

3.2 Cyclic liquefaction resistance

The cyclic resistance of granular materials under uniform amplitude of shearing (constant CSR) can be quantified by the number of loading cycles to initial liquefaction, or N_{IL}. More broadly, the liquefaction strength curve, which represents the relation between CSR and N_{IL}, is commonly used to represent the resistance of a granular system to cyclic liquefaction failure, and it bears significant practical implications. Figures 7 and 8 display the liquefaction strength curves of the ten samples prepared in this study. Each data point on these curves corresponds to a constant volume cyclic simple shear simulation conducted on a sample with a specific particle shape (AR and B) and D_{r}, as specified in Table 3. The discrete data points associated with the same sample are fitted using a power-law function:

$$\mathrm{CSR} \propto N_{\mathrm{IL}}^{-b} \tag{8}$$

with the exponent b being a fitting parameter. The fitted curves to the data points in Figs. 7 and 8 depict the liquefaction strength curves for each sample. Notably, the liquefaction strength curves for samples with $D_{\mathrm{r}} = 50\%$ are positioned in the upper right side of the plots, while those for samples with $D_{\mathrm{r}} = 20\%$ are located at the lower left side. This spatial distribution indicates that denser samples exhibit greater liquefaction resistance, in line with the expected behavior that increasing the relative density of granular assemblies typically enhances their liquefaction resistance.

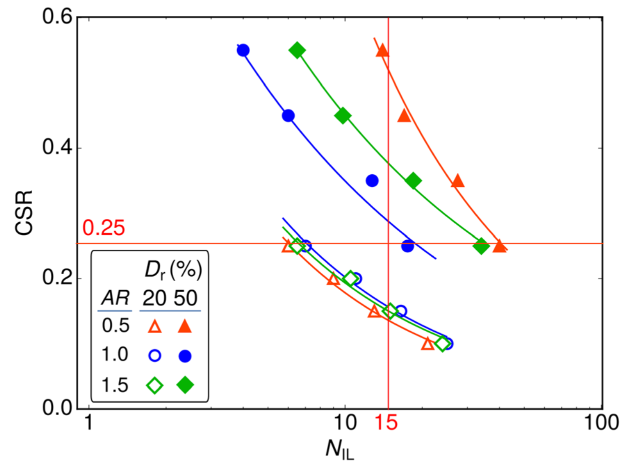

Fig. 7 Cyclic liquefaction strength curves for samples with different AR and D_{r} when $B = 2$. The solid curves are power-law fits to the data points. Solid lines at $N_{\mathrm{IL}} = 15$ and CSR $= 0.25$ inform the plots of cyclic liquefaction resistance in Fig. 9

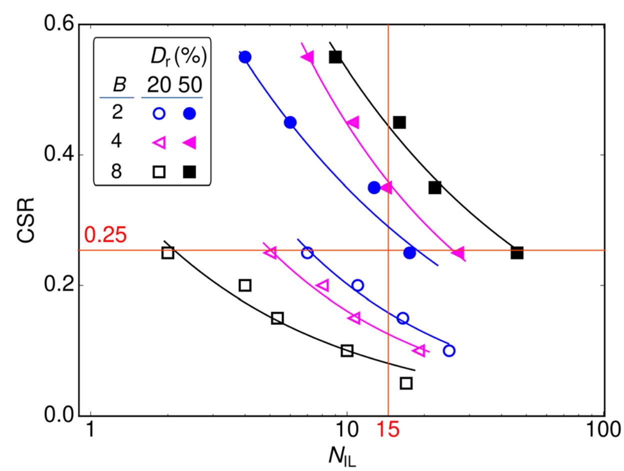

Fig. 8 Cyclic liquefaction strength curves for samples with different B and D_{r} when AR $= 1$. The solid curves are power-law fits to the data points. Solid lines at $N_{\mathrm{IL}} = 15$ and CSR $= 0.25$ inform the plots of cyclic liquefaction resistance in Fig. 9

The influence of AR on the position of the liquefaction strength curve in Fig. 7 exhibits a complex relation that depends on the relative density of the samples. For samples with $D_{\mathrm{r}} = 20\%$, the liquefaction strength curves appear to nearly overlap. However, upon closer examination, it becomes evident that the sphere exhibits the highest liquefaction resistance, followed by ellipsoidal particles with AR $= 1.5$ and then AR $= 0.5$. In contrast, for samples with $D_{\mathrm{r}} = 50\%$, the effect of AR is entirely reversed, and the difference is much more pronounced. In this case, the ellipsoidal particle with AR $= 0.5$ demonstrates the highest

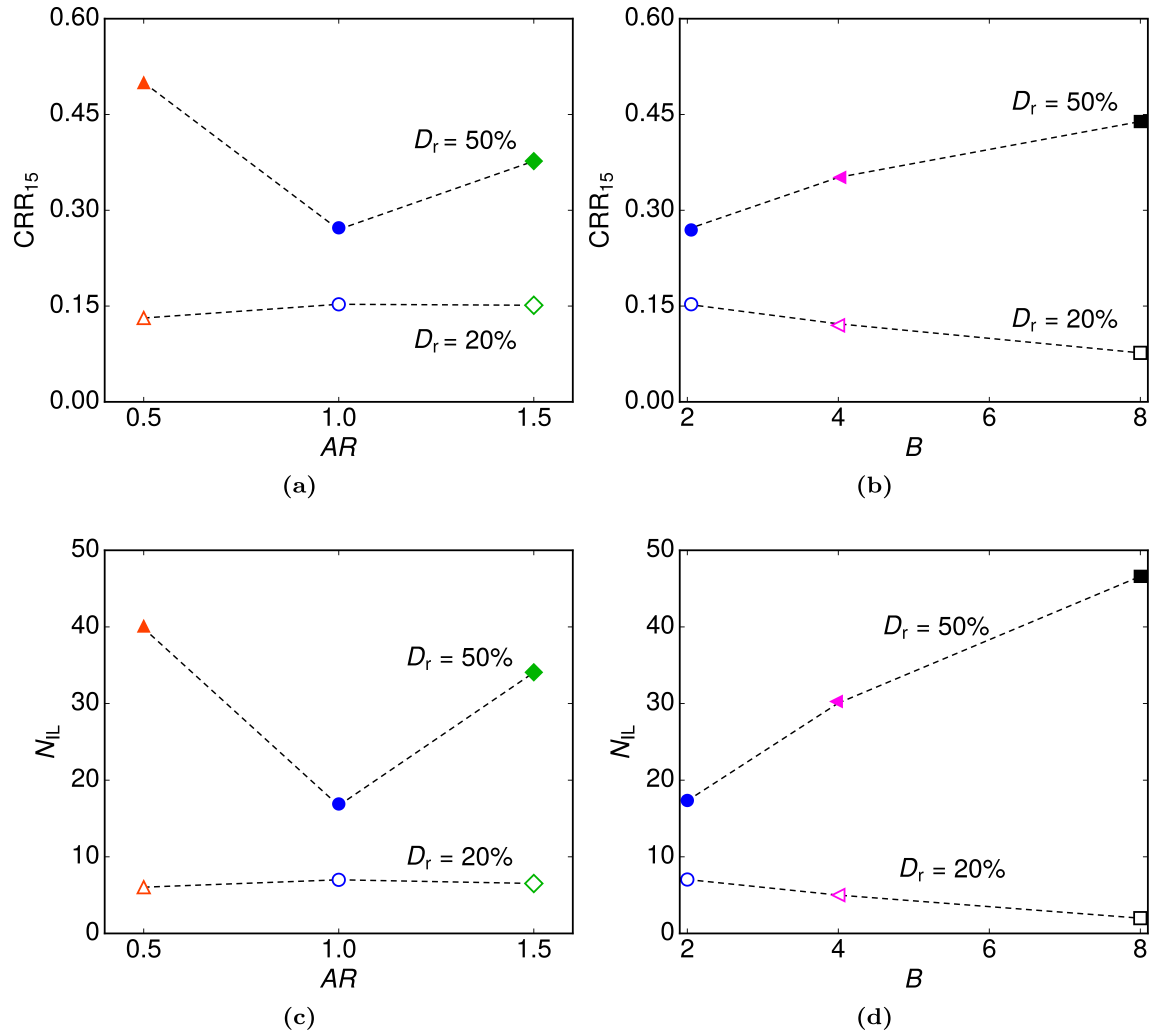

Fig. 9 Variations of cyclic liquefaction resistance in terms of **a, b** CRR_{15} and **c, d** N_{IL} for CSR = 0.25 against AR and B

liquefaction strength, followed by those with AR = 1.5, and finally, the spheres. Similar to AR, the effect of B on the liquefaction resistance also depends on the relative density of the samples. In Fig. 8, it can be observed that samples with $D_r = 20\%$ exhibit a decrease in liquefaction strength as B increases. This trend is reversed for samples with $D_r = 50\%$. In addition, interestingly, at lower D_r values, the effect of B on the liquefaction resistance is more pronounced than that of AR. Therefore, compared with non-spherical particles, the results indicate that spherical particles are more resistant to cyclic liquefaction at low relative densities and less resistant at high relative densities. The latter observation for samples at higher D_r is consistent with laboratory studies [e.g., 44, 48].

The cyclic liquefaction resistance of a sample is commonly defined in two ways based on the cyclic liquefaction curves: (a) the cyclic resistance ratio (CRR), which corresponds to the CSR required to induce initial liquefaction within a specific number of loading cycles (e.g., CRR_{15} represents the CSR necessary to initiate liquefaction in 15 loading cycles); and (b) the number of cycles (N_{IL}) required to reach initial liquefaction for a given CSR (e.g., N_{IL} for CSR = 0.25). The vertical and horizontal solid lines in Figs. 7 and 8 represent these two measures. The CRR_{15} is computed through the interpolation function of Eq. (8). Figure 9a, b presents the effects of AR and B on CRR_{15} for each of the two D_r levels. For samples with $D_r = 20\%$, the change in AR does not affect CRR_{15} noticeably, while an increase of B from 2 results in reduced CRR_{15}. For samples with $D_r = 50\%$, an increase in AR from 0.5 initially reduces CRR_{15} when AR = 1 and then increases CRR_{15}, while CRR_{15} and B presents a monotonically increasing relation. Similar observations can be made in Fig. 9c, d depicting the relation between N_{IL} for CSR = 0.25 and AR or B.

Recall from Fig. 2 showing the variations of roundness (R) and sphericity (S) for the superquadrics considered in this study. Instead of using AR and B, or R and S, a single

Table 4 Roundness, sphericity, and overall regularity of the particles considered in this study

AR	*B*	*R*	*S*	OR
0.5	2	0.67	0.50	0.59
1.0	2	1.00	1.00	1.00
1.5	2	0.92	0.67	0.79
1.0	4	0.50	0.79	0.64
1.0	8	0.25	0.63	0.44

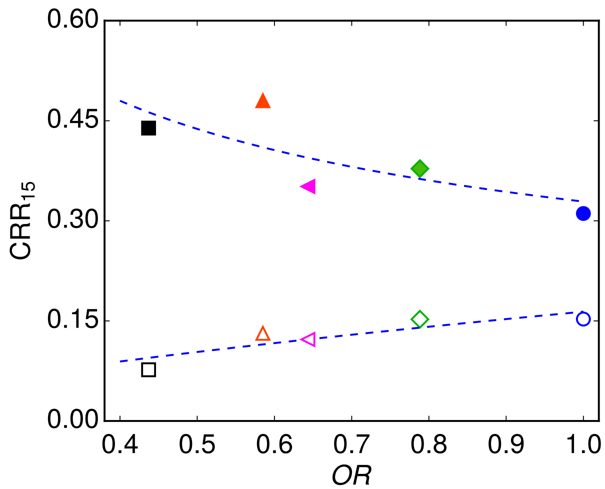

(a)

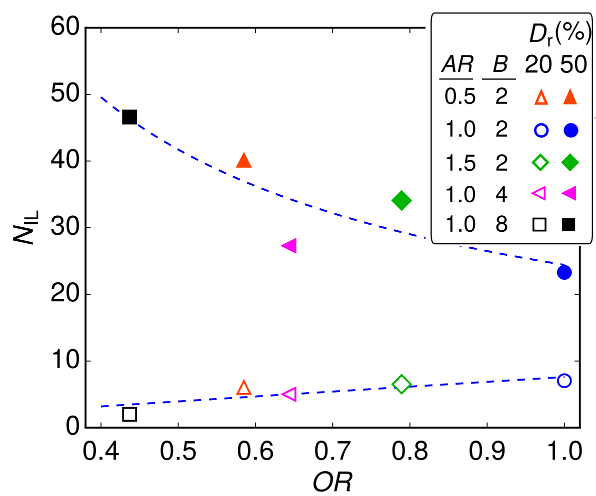

(b)

Fig. 10 Variation of the cyclic liquefaction resistance with the overall regularity (OR) with respect to **a** CRR_{15} and **b** N_{IL} for CSR = 0.25

shape parameter called overall regularity (OR), defined as $OR = (R + S)/2$, can be adopted to describe particle shape [14, 44]. Table 4 lists the OR values for the five superquadrics considered in this study, based on the data in Fig. 2. Clearly, the sphere presents the highest OR value. Generally, OR decreases with AR shifting away from 1 or increasing *B*.

Figure 10 presents the variations of cyclic liquefaction strength quantified by CRR_{15} and N_{IL} for $CSR = 0.25$ against OR. For samples with $D_r = 20\%$, liquefaction strength slightly increases with increasing OR. Conversely, for samples with $D_r = 50\%$, liquefaction strength noticeably decreases with increasing OR. These plots indicate a monotonic variation of cyclic liquefaction resistance with respect to OR.

4 Linking with the initial state

In this section, selected macro- and micro-scale descriptors have been used to evaluate the consistency of their trends with the observations related to particle shape influences on the cyclic liquefaction resistance, illustrated earlier in Fig. 10. The impact of OR on CRR_{15} is primarily assumed to be attributed to the inherent properties of the samples, focusing on the examination of the packing properties of the samples at the beginning of the constant-volume cyclic shearing stage. It is important to note that the differences in particle shape may lead to distinct patterns of evolution for these descriptors until the initial liquefaction state is reached. Consequently, this aspect warrants further assessment and investigation.

4.1 Initial coordination number

Following the same approach as in Banerjee et al. [7], the initial coordination number is adopted as a lowest-order scalar descriptor quantifying the packing contact network.

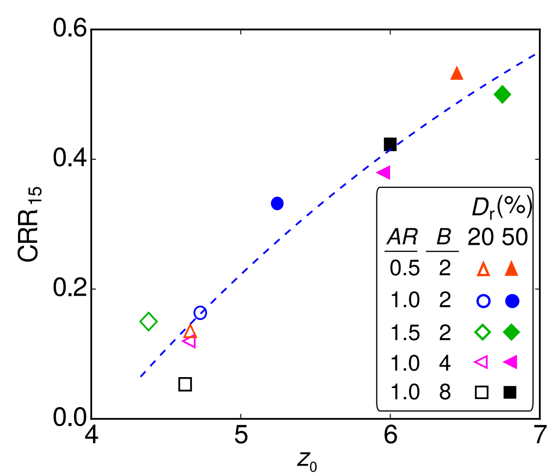

Fig. 11 The relation between CRR_{15} and z_0 for samples composed of distinct superquadric particles at different D_r

The average coordination number refers to the average number of contacts per particle and provides an approximation of the level of static redundancy within the granular system, i.e., the discrepancy between the number of constraints and the number of degrees of freedom [46]. To ensure a meaningful representation of the stable state of stress, particles with zero or only one contact are excluded when defining the mechanical coordination number [47]. This exclusion is justified by the fact that such particles do not contribute to the extension of the contact network and, therefore, do not significantly influence the overall stress equilibrium. The mechanical coordination number is defined as

$$z = \frac{2N_c - N_p^1}{N_p - N_p^0 - N_p^1}, \quad (9)$$

where N_c and N_p are the numbers of contacts and particles, respectively, and N_p^0, N_p^1 are the numbers of particles with zero or only one contact, respectively. The sixth column of Table 2 presents the initial mechanical coordination number z_0 of the samples prepared in this study.

Figure 11 illustrates the variations of the deduced CRR_{15} with respect to z_0. The dashed curve represents the exponential function fit to the ten data points, revealing a somewhat monotonic relation between CRR15 and z_0. This relation suggests that isotropically compressed samples with a higher initial mechanical coordination number tend to exhibit greater cyclic liquefaction resistance. Consequently, it can be inferred that the connection between particle shape and liquefaction strength arises from the particle shape effect on the distinct packing properties. Notably, in these samples following a similar preparation protocol, it is observed that the sample composed of spheres exhibits the highest initial mechanical coordination number (z_0) for $D_\mathrm{r} = 20\%$ and the lowest z_0 value for $D_\mathrm{r} = 50\%$, corresponding to the highest and lowest liquefaction resistance, respectively. It should be noted that the relation between CRR_{15} and z_0 depicted in Fig. 11 is not strictly rigorous as certain discrepancies can be identified. For instance, at $D_\mathrm{r} = 20\%$, the sample with $\mathrm{AR} = 1$ and $B = 8$ exhibits a higher z_0 value compared to the sample with $\mathrm{AR} = 1.5$ and $B = 2$, but presents a lower CRR_{15} value. Counterexamples like this highlight the need for further investigation of contact types [e.g., 5], as particle shape may impact the role of the contacts in the stability of the granular system. Alternatively, exploration of other descriptors that may better correlate with the deduced CRR_{15} within the ranges of particle shape and D_r considered in this study is warranted.

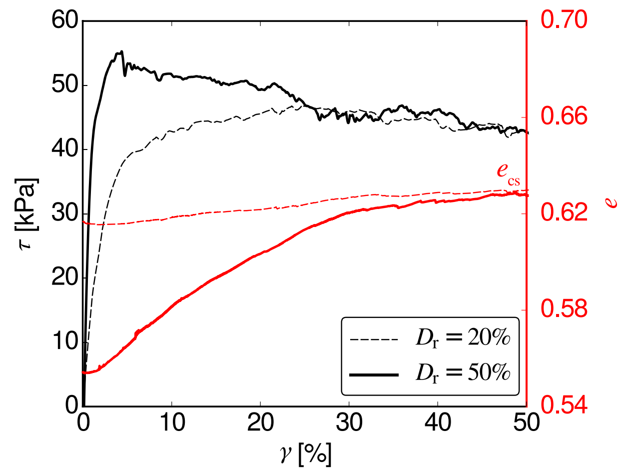

(a)

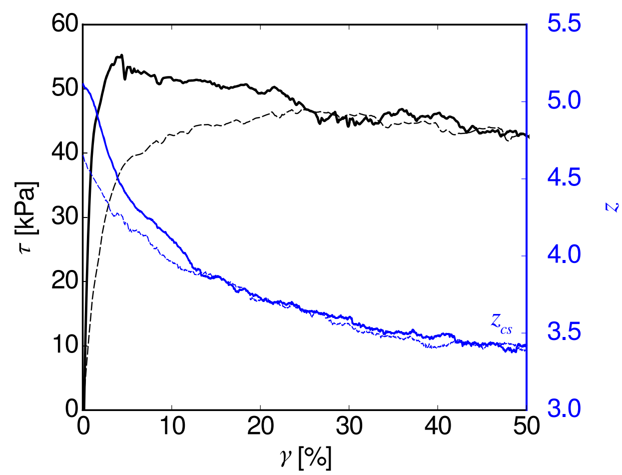

(b)

Fig. 12 Evolutions of shear stress τ, void ratio e, and mechanical coordination number z with applied shear strain in drained constant-p monotonic simple shear tests on the samples with AR = 1, B = 2 and different D_r

4.2 Initial state parameter

The state parameter, a widely used macroscopic measure closely associated with the shear response of sands, combines the influence of void ratio and stress level relative to an ultimate (steady) state to describe the behavior. The state parameter ψ, introduced by Been and Jefferies [24], represents the difference between the current void ratio e and the critical state void ratio e_cs at the same mean stress p, expressed as $e - e_\mathrm{cs}$. Let us refer to this void ratio-based state parameter as ψ_e, and its initial value at the beginning of the constant volume cyclic shearing stage as $\psi_{e,0}$. Several recent studies have suggested a decrease in cyclic liquefaction resistance with an increase in the initial state parameter $\psi_{e,0}$, despite some scattering observed in laboratory experimental data [e.g., 24, 57, 40]. Notably, a

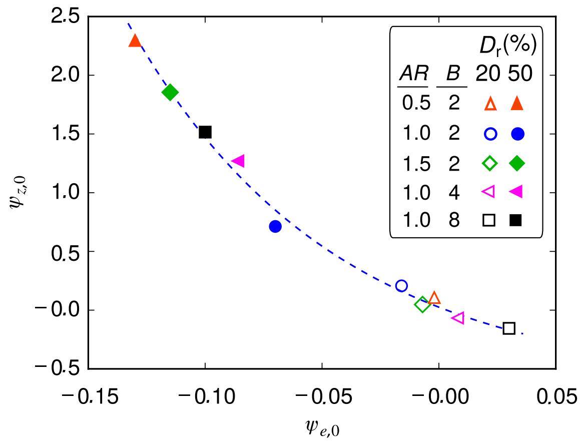

Fig. 13 The relation between $\psi_{z,0}$ and $\psi_{e,0}$ for samples composed of distinct superquadric particles at different D_r

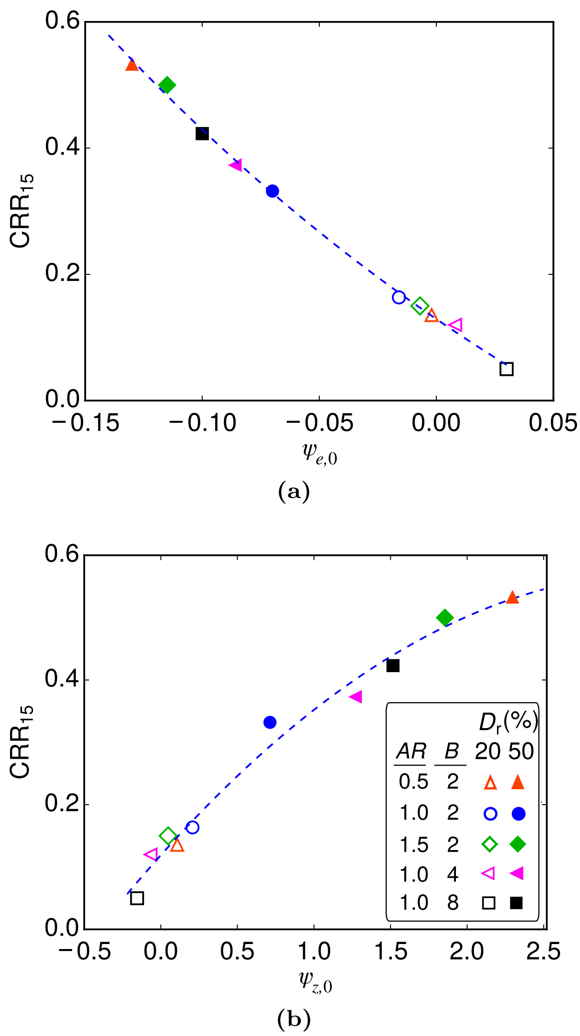

Fig. 14 Variations of cyclic liquefaction resistance CRR_{15} against **a** initial value of macro state parameter $\psi_{e,0}$ and **b** initial value of micro state parameter $\psi_{z,0}$, for samples composed of distinct superquadric particles at different D_r

similar trend has also been observed in recent DEM studies [e.g., 20, 41, 7].

Following a similar approach to defining ψ_e, one can introduce a micro state parameter, denoted as ψ_z, which represents the difference between the current mechanical coordination number z and the critical state mechanical coordination number z_{cs} corresponding to the same mean stress p. In other words, ψ_z is defined as $z - z_{cs}$. Let us refer to the initial value of this mechanical coordination number-based micro state parameter as $\psi_{z,0}$. Some recent DEM studies [7, 20, 58] suggest the potential advantages of using such a micro state parameter, rather than the more conventional macro state parameter, for correlating with the cyclic liquefaction resistance. In this study, the applicability and effectiveness of this micro state parameter will be evaluated for the samples under consideration in this study.

To determine the values of $\psi_{e,0}$ and $\psi_{z,0}$ for each sample in this study, the e_{cs} and z_{cs} values corresponding to the initial confinement p_0 are necessary. To readily achieve these values, Banerjee et al. [7] proposed a special strain control constant-p shearing protocol. In this protocol, while using bi-periodic boundary conditions for the lateral sides of the sample box, the normal stresses σ_{xx}, σ_{yy}, and σ_{zz}, are kept constant using a servo-control algorithm, hence $\dot{p} = 0$, and the sample is sheared under a constant shear velocity applied to the top wall along the x direction, hence a shear strain rate $\dot{\gamma}$ within the sample. As a result, shear stress varies until the sample reaches a state close to the critical state, where the shear stress τ and the void ratio e reach a nearly steady state. The corresponding values of void ratio and coordination number at this state are denoted as e_{cs} and z_{cs}. Table 2 lists these values for all ten samples. Figure 12 shows the evolutions of the shear stress, void ratio, and mechanical coordination number for samples composed of spheres at two relative densities, leading to the values of e_{cs} and z_{cs}. As anticipated, unique values of τ, e_{cs}, and z_{cs} are obtained at sufficiently large levels of shear strain γ for samples with different initial relative densities but the same particle shape.

The resulting values of $\psi_{e,0}$ and $\psi_{z,0}$ for samples with different particle shapes and D_r are presented in Fig. 13, revealing a unique relation between these two quantities. A monotonic relation between CRR_{15} and $\psi_{e,0}$ is depicted in Fig. 14a, where the data points are fitted using an exponential function. This observation aligns with previous studies [7, 20, 42, 57], which focused on factors other than particle shape. Therefore, these results demonstrate the feasibility of linking cyclic liquefaction resistance with the initial state parameter, even when considering samples with different particle shapes. Similarly, Fig. 14b illustrates the relation between CRR_{15} and $\psi_{z,0}$, also fitted with an exponential function. The CRR_{15} decreases nonlinearly as $\psi_{e,0}$ increases or $\psi_{z,0}$ decreases. In comparison with the CRR_{15}–z_0 relation in Fig. 11, the data points in Fig. 14b are positioned closer to the fitting curve and present fewer counter-examples against the presumed monotonic relation. The improved performance of $\psi_{z,0}$ compared to z_0 in correlating with CRR_{15} can be attributed to the incorporation of z_{cs}, which serves as a reference and normalizes z_0. It is noteworthy that in Fig. 14, there is no clear superiority of $\psi_{z,0}$ over CRR_{15} in terms of their correlation with CRR_{15}.

5 Conclusions

In this study, a three-dimensional discrete element method was adopted to investigate the effect of particle shape on the cyclic liquefaction resistance of granular materials. To account for particle shape, a family of superquadric particles was utilized, including ellipsoids with varying aspect ratios (AR) and blocky particles with different blockiness values (B). Five smooth and convex particle shapes were employed, consisting of different combinations of AR and B values, covering AR $= 0.5$ and $B = 2$, AR $= 1$ and $B = 2$, AR $= 1.5$ and $B = 2$, AR $= 1$ and $B = 4$, and AR $= 1$ and $B = 8$. These distinct particles were then used to construct isotropically compressed samples under an initial confinement of 100 kPa at relative densities of 20% and 50%. Subsequently, the samples were subjected to unidirectional cyclic simple shear with different levels of uniform cyclic stress ratio (CSR) until reaching the initial liquefaction state.

The findings indicate that at each level of relative density studied, the effects of AR and B on the cyclic liquefaction resistance do not exhibit a monotonic trend. To facilitate the assessment of the particle shape effect, the cyclic resistance ratio CRR_{15} was adopted as a measure of cyclic liquefaction resistance. At $D_r = 20\%$, CRR_{15} remains relatively constant as AR increases with $B = 2$. However, with AR $= 1$ and increasing B, CRR_{15} decreases. At $D_r = 50\%$, for $B = 2$, the spherical particle displays the lowest liquefaction resistance, followed by AR $= 1.5$ and AR $= 0.5$. Conversely, with AR $= 1$, CRR_{15} increases with increasing B. When incorporating the overall regularity (OR) to synchronize the shape descriptions, it is observed that for samples with D_r, CRR_{15} demonstrates an approximate increasing trend as OR increases. However, this trend is reversed for samples with $D_r = 50\%$.

To establish a connection between the macroscopic observations and the initial state, initial values of both macro- and micro-scale descriptors were extracted from the samples before undergoing cyclic shearing. The initial mechanical coordination number exhibits a discernible trend with the resulting CRR_{15}, despite some scattered data points. Additionally, two types of state parameters associated with the macro void ratio and micromechanical coordination number, denoted as $\psi_{e,0}$ and $\psi_{z,0}$, respectively, demonstrate a consistent monotonic relation with CRR_{15}, regardless of relative density and particle shape. This suggests that the influence of particle shape on cyclic liquefaction resistance can be attributed to its direct impact on the packing properties of the sample. Furthermore, it raises the question of how particle shape affects the evolution of microstructure as the sample approaches initial liquefaction. Exploring this aspect would provide additional insights into the effect of particle shape on cyclic liquefaction resistance. This area, which has not been fully investigated, merits further evaluation in future studies.

Acknowledgements Financial support for this study was provided by the Natural Sciences and Engineering Research Council of Canada (NSERC). We thank Prof. Ellen Rathje for facilitating our access to HPC resources at the Texas Advanced Computing Center. We also thank Dr. Eric Breard for sharing a ray tracing script used in preparing Fig. 4.

Data availability The datasets generated during and/or analyzed during the current study are available from the corresponding author on reasonable request.

Declarations

Conflict of interest The authors declare that they have no conflict of interest.

References

1. Agnolin I, Roux JN (2007) Internal states of model isotropic granular packings. I. Assembling process, geometry, and contact networks. Phys Rev E 76(6):061302. https://doi.org/10.1103/PhysRevE.76.061302
2. Ai J, Chen JF, Rotter JM, Ooi JY (2011) Assessment of rolling resistance models in discrete element simulations. Powder Technol 206(3):269–282. https://doi.org/10.1016/j.powtec.2010.09.030
3. Ashmawy AK, Hoang VV, Sukumaran B (2003) Evaluating the influence of particle shape on liquefaction behavior using discrete element modeling. In: The thirteenth international offshore and polar engineering conference, Honolulu, Hawaii, USA. International Society of Offshore and Polar Engineers, pp 542–549
4. Azéma E, Radjaï F (2010) Stress-strain behavior and geometrical properties of packings of elongated particles. Phys Rev E 81(5):051304. https://doi.org/10.1103/PhysRevE.81.051304
5. Azéma E, Radjai F, Dubois F (2013) Packings of irregular polyhedral particles: Strength, structure, and effects of angularity. Phys Rev E 87(6):062203. https://doi.org/10.1103/PhysRevE.87.062203
6. Banerjee S (2022) Effects of particle size distribution and particle shape on cyclic liquefaction response of granular materials. Ph.D. thesis, The University of British Columbia, Vancouver, Canada. https://doi.org/10.14288/1.0413026

7. Banerjee SK, Yang M, Taiebat M (2023) Effect of coefficient of uniformity on cyclic liquefaction resistance of granular materials. Comput Geotech 155:105232. https://doi.org/10.1016/j.compgeo.2022.105232
8. Barr AH (1981) Superquadrics and angle-preserving transformations. IEEE Comput Graph Appl 1(1):11–23. https://doi.org/10.1109/MCG.1981.1673799
9. Barrero AR, Taiebat M, Dafalias YF (2020) Modeling cyclic shearing of sands in the semifluidized state. Int J Numer Anal Methods Geomech 44(3):371–388. https://doi.org/10.1002/nag.3007
10. Berry N, Zhang Y, Haeri S (2021) Lees–Edwards boundary conditions for the multi-sphere discrete element method. Powder Technol 389:292–308. https://doi.org/10.1016/j.powtec.2021.05.025
11. Bonilla RRO (2004) Numerical simulations of undrained granular media. Ph.D. thesis, University of Waterloo, Waterloo, Canada
12. Castro G, Poulos SJ (1977) Factors affecting liquefaction and cyclic mobility. J Geotech Eng Div 103(6):501–516. https://doi.org/10.1061/AJGEB6.0000433
13. Chiaro G, Koseki J, Sato T (2012) Effects of initial static shear on liquefaction and large deformation properties of loose saturated Toyoura sand in undrained cyclic torsional shear tests. Soils Found 52(3):498–510. https://doi.org/10.1016/j.sandf.2012.05.008
14. Cho GC, Dodds J, Santamarina JC (2006) Particle shape effects on packing density, stiffness, and strength: natural and crushed sands. J Geotech Geoenviron Eng 132(5):591–602. https://doi.org/10.1061/(ASCE)1090-0241(2006)132:5(591)
15. Duque J, Yang M, Fuentes W, Mašín D, Taiebat M (2021) Characteristic limitations of advanced plasticity and hypoplasticity models for cyclic loading of sands. Acta Geotech 17(6):2235–2257. https://doi.org/10.1007/s11440-021-01418-z
16. Dyvik R, Lacasse S, Berre T, Raadim B (1987) Comparison of truly undrained and constant volume direct simple shear tests. Géotechnique 37(1):3–10. https://doi.org/10.1680/geot.1987.37.1.3
17. Estrada N, Taboada A, Radjai F (2008) Shear strength and force transmission in granular media with rolling resistance. Phys Rev E 78(2):021301. https://doi.org/10.1103/PhysRevE.78.021301
18. Feng Y (2023) Thirty years of developments in contact modelling of non-spherical particles in dem: a selective review. Acta Mech Sin 39(1):722343. https://doi.org/10.1007/s10409-022-22343-x
19. Ferellec JF, McDowell GR (2010) A method to model realistic particle shape and inertia in DEM. Granul Matter 12(5):459–467. https://doi.org/10.1007/s10035-010-0205-8
20. Gu X, Zhang J, Huang X (2020) DEM analysis of monotonic and cyclic behaviors of sand based on critical state soil mechanics framework. Comput Geotech 128:103787. https://doi.org/10.1016/j.compgeo.2020.103787
21. Hart R, Cundall PA, Lemos J (1988) Formulation of a three-dimensional distinct element model-Part II. Mechanical calculations for motion and interaction of a system composed of many polyhedral blocks. Int J Rock Mech Min Sci Geomech Abstr 25(3):117–125. https://doi.org/10.1016/0148-9062(88)92294-2
22. Hubler JF, Athanasopoulos-Zekkos A, Zekkos D (2017) Monotonic, cyclic, and postcyclic simple shear response of three uniform Gravels in constant volume conditions. J Geotech Geoenviron Eng 143(9):04017043. https://doi.org/10.1061/(ASCE)GT.1943-5606.0001723
23. Ishihara K (1993) Liquefaction and flow failure during earthquakes. Géotechnique 43(3):351–451. https://doi.org/10.1680/geot.1993.43.3.351
24. Jefferies M, Been K (2015) Soil liquefaction: a critical state approach. CRC Press. https://doi.org/10.1201/b19114
25. Jerves AX, Kawamoto RY, Andrade JE (2016) Effects of grain morphology on critical state: a computational analysis. Acta Geotech 11(3):493–503. https://doi.org/10.1007/s11440-015-0422-8
26. Jostad HP, Khoa H, Karapiperis K, Andrade J (2021) Can LS-DEM be used to simulate cyclic behavior of sand? In: Challenges and innovations in geomechanics: proceedings of the 16th international conference of IACMAG, volume 1 16. Springer, pp 228–235
27. Kawamoto R, Andò E, Viggiani G, Andrade JE (2016) Level set discrete element method for three-dimensional computations with triaxial case study. J Mech Phys Solids 91:1–13. https://doi.org/10.1016/j.jmps.2016.02.021
28. Kloss C, Goniva C, Hager A, Amberger S, Pirker S (2012) Models, algorithms and validation for opensource DEM and CFD-DEM. Progress Comput Fluid Dyn Int J 12(2–3):140–152. https://doi.org/10.1504/PCFD.2012.047457
29. Kuhn MR, Renken HE, Mixsell AD, Kramer SL (2014) Investigation of cyclic liquefaction with discrete element simulations. J Geotech Geoenviron Eng 140(12):04014075. https://doi.org/10.1061/(ASCE)GT.1943-5606.0001181
30. Lees AW, Edwards SF (1972) The computer study of transport processes underextreme conditions. J Phys C Solid State Phys 5:1921. https://doi.org/10.1088/0022-3719/5/15/006
31. Lim KW, Andrade JE (2014) Granular element method for three-dimensional discrete element calculations. Int J Numer Anal Methods Geomech 38(2):167–188. https://doi.org/10.1002/nag.2203
32. Limnaiou TG, Papadimitriou AG (2022) Bounding surface plasticity model with reversal surfaces for the monotonic and cyclic shearing of sands. Acta Geotech 18(1):235–263. https://doi.org/10.1007/s11440-022-01529-1
33. Martin EL, Thornton C, Utili S (2020) Micromechanical investigation of liquefaction of granular media by cyclic 3D DEM tests. Géotechnique 70(10):906–915. https://doi.org/10.1680/jgeot.18.P.267
34. MiDi GDR (2004) On dense granular flows. Eur Phys J E 14(4):341–365. https://doi.org/10.1140/epje/i2003-10153-0
35. Morimoto T, Otsubo M, Koseki J (2021) Microscopic investigation into liquefaction resistance of pre-sheared sand: effects of particle shape and initial anisotropy. Soils Found 61(2):335–351. https://doi.org/10.1016/j.sandf.2020.12.008
36. Mutabaruka P, Taiebat M, Pellenq RJM, Radjai F (2019) Effects of size polydispersity on random close-packed configurations of spherical particles. Phys Rev E 100(4):042906. https://doi.org/10.1103/PhysRevE.100.042906
37. Nguyen HBK, Rahman MM, Fourie AB (2021) How particle shape affects the critical state, triggering of instability and dilatancy of granular materials-results from a DEM study. Géotechnique 71(9):749–764. https://doi.org/10.1680/jgeot.18.P.211
38. Park SS, Nong ZZ, Doan NP (2022) Constitutive modeling of principal stress rotation associated with sand under simple shear loading. Int J Numer Anal Methods Geomech 46(8):1494–1524. https://doi.org/10.1002/nag.3354
39. Podlozhnyuk A, Pirker S, Kloss C (2017) Efficient implementation of superquadric particles in Discrete Element Method within an open-source framework. Comput Part Mech 4(1):101–118. https://doi.org/10.1007/s40571-016-0131-6
40. Porcino DD, Triantafyllidis T, Wichtmann T, Tomasello G (2021) Application of critical state approach to liquefaction resistance of sand-silt mixtures under cyclic simple shear loading. J Geotech Geoenviron Eng 147(3):04020177. https://doi.org/10.1061/(ASCE)GT.1943-5606.0002470
41. Rahman M, Nguyen H, Fourie A, Kuhn M (2021) Critical state soil mechanics for cyclic liquefaction and postliquefaction behavior: DEM study. J Geotech Geoenviron Eng

147(2):04020166. https://doi.org/10.1061/(ASCE)GT.1943-5606.0002453

42. Rahman MM, Sitharam T (2020) Cyclic liquefaction screening of sand with non-plastic fines: critical state approach. Geosci Front 11(2):429–438. https://doi.org/10.1016/j.gsf.2018.09.009
43. Rathje EM, Dawson C, Padgett JE, Pinelli JP, Stanzione D, Adair A, Arduino P, Brandenberg SJ, Cockerill T, Dey C et al (2017) Designsafe: new cyberinfrastructure for natural hazards engineering. Nat Hazard Rev 18(3):06017001. https://doi.org/10.1061/(ASCE)NH.1527-6996.0000246
44. Rui S, Guo Z, Si T, Li Y (2020) Effect of particle shape on the liquefaction resistance of calcareous sands. Soil Dyn Earthq Eng 137:106302. https://doi.org/10.1016/j.soildyn.2020.106302
45. Taiebat M, Mutabaruka P, Pellenq R, Radjaï F (2017) Effect of particle size distribution on 3D packings of spherical particles. EPJ Web Conf 140:02030. https://doi.org/10.1051/epjconf/201714002030
46. Thornton C (2015) Granular dynamics, contact mechanics and particle system simulations: A DEM study. Part Technol Ser 24. https://doi.org/10.1007/978-3-319-18711-2
47. Thornton C (2000) Numerical simulations of deviatoric shear deformation of granular media. Géotechnique 50(1):43–53. https://doi.org/10.1680/geot.2000.50.1.43
48. Vaid YP, Chern JC, Tumi H (1985) Confining pressure, grain angularity, and liquefaction. J Geotech Eng 111(10):1229–1235. https://doi.org/10.1061/(ASCE)0733-9410(1985)111:10(1229)
49. Vargas RR, Ueda K, Uemura K (2020) Influence of the relative density and K_0 effects in the cyclic response of Ottawa F-65 sand-cyclic Torsional Hollow-Cylinder shear tests for LEAP-ASIA-2019. Soil Dyn Earthq Eng 133:106111. https://doi.org/10.1016/j.soildyn.2020.106111
50. Wadell H (1932) Volume, shape, and roundness of rock particles. J Geol 40(5):443–451. https://doi.org/10.1086/623964
51. Wang Z, Yang Y, Li Y, Liu S, Zhou P (2022) Numerical simulation of cyclic shear tests considering the fabric change and principal stress rotation effects. Int J Numer Anal Methods Geomech 46(8):1409–1432. https://doi.org/10.1002/nag.3351
52. Wei X, Yang J, Zhuang YS, Zhou YG, Chen YM (2019) Effects of particle shape on the liquefaction resistance of sands. In: Earthquake geotechnical engineering for protection and development of environment and constructions. CRC Press, pp 5656–5663
53. Wensrich C, Katterfeld A (2012) Rolling friction as a technique for modelling particle shape in DEM. Powder Technol 217:409–417. https://doi.org/10.1016/j.powtec.2011.10.057
54. Wichtmann T, Triantafyllidis T (2016) An experimental database for the development, calibration and verification of constitutive models for sand with focus to cyclic loading: part I-tests with monotonic loading and stress cycles. Acta Geotech 11(4):739–761. https://doi.org/10.1007/s11440-015-0402-z
55. Williams JR, Pentland AP (1992) Superquadrics and modal dynamics for discrete elements in interactive design. Eng Comput 9(2):115–127. https://doi.org/10.1108/eb023852
56. Xie Y, Yang Z, Barreto D, Jiang M (2017) The influence of particle geometry and the intermediate stress ratio on the shear behavior of granular materials. Granul Matter 19:1–13. https://doi.org/10.1007/s10035-017-0723-8
57. Yang J, Sze HY (2011) Cyclic behaviour and resistance of saturated sand under non-symmetrical loading conditions. Géotechnique 61(1):59–73. https://doi.org/10.1680/geot.9.P.019
58. Yang M, Taiebat M (2024) Effect of anisotropic consolidation on cyclic liquefaction resistance of granular materials via 3D-DEM modeling. J Geotech Geoenviron Eng. https://doi.org/10.1061/jggefk/gteng-11970
59. Yang M, Taiebat M, Dafalias YF (2022) SANISAND-MSf: a sand plasticity model with memory surface and semifluidised state. Géotechnique 72(3):227–246. https://doi.org/10.1680/jgeot.19.p.363
60. Yang M, Taiebat M, Mutabaruka P, Radjaï F (2021) Evolution of granular materials under isochoric cyclic simple shearing. Phys Rev E 103(3):032904. https://doi.org/10.1103/PhysRevE.103.032904
61. Yang M, Taiebat M, Mutabaruka P, Radjaï F (2021) Geometrical network of granular materials under isochoric cyclic shearing. EPJ Web Conf 249:11004. https://doi.org/10.1051/epjconf/202124911004
62. Yang M, Taiebat M, Mutabaruka P, Radjaï F (2022) Evolution of granular media under constant-volume multidirectional cyclic shearing. Acta Geotech 17:779–802. https://doi.org/10.1007/s11440-021-01239-0
63. Yang M, Taiebat M, Radjaï F (2022) Liquefaction of granular materials in constant-volume cyclic shearing: transition between solid-like and fluid-like states. Comput Geotech 148:104800. https://doi.org/10.1016/j.compgeo.2022.104800
64. Zhang A, Jiang M, Thornton C (2019) A coupled CFD-DEM method with moving mesh for simulating undrained triaxial tests on granular soils. Granul Matter 22(1):25. https://doi.org/10.1007/s10035-019-0984-5
65. Zhang W, Rothenburg L (2020) Comparison of undrained behaviors of granular media using fluid-coupled discrete element method and constant volume method. J Rock Mech Geotech Eng 12(6):1272–1289. https://doi.org/10.1016/j.jrmge.2020.03.009